

Supersymmetry-driven segmented tapered laser for stabilized single transverse and longitudinal mode engineering

Yiwen Lou(楼亦文), Tian Lan(兰天), Jun Qi(齐军), Jinlong Zhao(赵金龙), Ying Li(李颖), Baiyi Qin(覃柏颐), Yuying Liu(刘豫颖), Xuesheng Liu(刘学胜), and Zhiyong Wang (王智勇)

Citation: Chin. Phys. B, 2026, 35 (**4**): 044207. DOI: 10.1088/1674-1056/ae29f9
http://cpb.iphy.ac.cn; http://iopscience.iop.org/cpb

What follows is a list of articles you may be interested in

Dissipative soliton resonance within different dispersion regimes in a single mode-locked laser

Zhetao Zhao(赵哲韬), Qinke Shu(舒沁珂), Ziyi Xie(解梓怡), Yuxuan Ren(任俞宣), Ying Zhang(张颖), Bo Yuan(袁博), Chunbo Zhao(赵春勃), Junsong Peng(彭俊松), and Heping Zeng(曾和平)
Chin. Phys. B, 2024, 33 (**7**): 074208. DOI: 10.1088/1674-1056/ad47b1

Optically pumped wavelength-tunable lasing from a GaN beam cavity with an integrated Joule heater pivoted on Si

Feifei Qin(秦飞飞), Yang Sun(孙阳), Ying Yang(杨颖), Xin Li(李欣), Xu Wang(王旭), Junfeng Lu(卢俊峰), Yongjin Wang(王永进), and Gangyi Zhu(朱刚毅)
Chin. Phys. B, 2023, 32 (**5**): 054210. DOI: 10.1088/1674-1056/acc05e

Mode characteristics of VCSELs with different shape and size oxidation apertures

Xin-Yu Xie(谢新宇), Jian Li(李健), Xiao-Lang Qiu(邱小浪), Yong-Li Wang(王永丽), Chuan-Chuan Li(李川川), and Xin Wei(韦欣)
Chin. Phys. B, 2023, 32 (**4**): 044206. DOI: 10.1088/1674-1056/ac9821

Single-mode lasing in a coupled twin circular-side-octagon microcavity

Ke Yang(杨珂), Yue-De Yang(杨跃德), Jin-Long Xiao(肖金龙), and Yong-Zhen Huang(黄永箴)
Chin. Phys. B, 2022, 31 (**9**): 094205. DOI: 10.1088/1674-1056/ac6802

Spatial and spectral filtering of tapered lasers by using tapered distributed Bragg reflector grating

Jing-Jing Yang(杨晶晶), Jie Fan(范杰), Yong-Gang Zou(邹永刚),Hai-Zhu Wang(王海珠), and Xiao-Hui Ma(马晓辉)
Chin. Phys. B, 2022, 31 (**8**): 084203. DOI: 10.1088/1674-1056/ac5391

Supersymmetry-driven segmented tapered laser for stabilized single transverse and longitudinal mode engineering

Yiwen Lou(楼亦文)[1,2], Tian Lan(兰天)[1,2,†], Jun Qi(齐军)[1,2], Jinlong Zhao(赵金龙)[1,2], Ying Li(李颖)[3], Baiyi Qin(覃柏颐)[1,2], Yuying Liu(刘豫颖)[1,2], Xuesheng Liu(刘学胜)[1,2,‡], and Zhiyong Wang (王智勇)[1,2]

[1] *Institute of Advanced Technology on Semiconductor Optics & Electronics, Physics and Optoelectronic Engineering, Beijing University of Technology, Beijing* 100124, *China*

[2] *Key Laboratory of Trans-scale Laser Manufacturing Technology (Beijing University of Technology), Ministry of Education, Beijing* 100124, *China*

[3] *Beijing Institute of Radio Metrology and Measurement, Beijing* 100124, *China*

(Received 27 August 2025; revised manuscript received 23 November 2025; accepted manuscript online 9 December 2025)

Tapered lasers are extensively employed in high power single-mode lasing, yet still suffering from the potential formation of higher-order transverse modes in the tapered region, which severely degrades the laser beam quality. Herein, we propose a novel supersymmetric segmented tapered laser to achieve stable fundamental transverse mode operation. Our design features a three-segmented tapered waveguide along the light propagation direction, with sub-waveguides of varying widths flanking each main waveguide segment. The main waveguides measure 8 μm, 12 μm, and 16 μm in width. Specifically, the 8 μm main waveguide has a corresponding subsidiary waveguide of 2.67 μm; the 12 μm main waveguide has two subsidiary waveguides measuring 4.82 μm and 6.63 μm; and the 16 μm main waveguide has two subsidiary waveguides measuring 7.13 μm and 3.68 μm. Using the coupled-mode theory, we systematically analyzed the coupling coefficients under different inter-waveguide spacings, leading to an optimized spacing of 1.2 μm through comprehensive theoretical simulations and fabrication compatibility constraints. Furthermore, phase-shifted gratings were integrated between tapered waveguide segments to enable precise longitudinal mode selection. This synergistic design could successfully realize robust single-mode operation, offering a scalable framework for on-chip integrated high-power, high-beam-quality tapered lasers.

Keywords: supersymmetric theory, phase-shifted gratings, tapered laser, single mode

PACS: 42.55.–f, 42.60.–v, 42.55.Px

DOI: 10.1088/1674-1056/ae29f9 **CSTR:** 32038.14.CPB.ae29f9

1. Introduction

Single-mode lasing is a pivotal performance metric for edge-emitting semiconductor lasers (EELs), critical for applications requiring high beam quality such as coherent optical communication and precision sensing. However, conventional EELs with ridge waveguides face inherent limitations: the ridge width is constrained by single-mode cutoff conditions, leading to a small emission area at the cavity facet. This increases susceptibility to catastrophic optical damage (COD).[1–7] Additionally, the narrow ridge structure restricts the current injection region, limiting the output power. To address these issues, a tapered waveguide has been employed to amplify the optical power while maintaining the beam quality and enlarging the emission area to prevent COD.[8–14]

In recent years, research efforts on tapered lasers are dedicated to achieving high-power and high-brightness laser output. For traditional tapered lasers, Man *et al*. fabricated a 975 nm tapered laser with separate electrodes using a flip-chip mounting approach. When currents of 400 mA and 7 A were injected into the ridge section and the taper section, respectively, the device achieved a continuous-wave output power of 6.4 W. The beam quality factor was measured as $M^2 = 1.66(1/e^2)$, and the brightness reached 369 mW·cm^2·sr^{-1}.[14] These results demonstrate that separately driving the ridge and tapered sections enhances the output beam quality of the device. On the other hand, Yang *et al*. fabricated a 1064 nm T-DBR tapered laser. By optimizing the grating design and fabrication process, they achieved single-lobe emission with a linewidth of 56 pm and an M^2 factor of 1.38. Under pulsed operation with a 5 ns pulse width and 200 kHz repetition rate, the device delivered an output peak power of 8.64 W.[17] Nevertheless, during operation, tapered lasers still exhibit multimode instabilities as higher-order transverse modes emerge in the tapered region, disrupting fundamental mode output. Existing approaches to suppressing higher-order modes include etching isolation trenches alongside ridge waveguides to attenuate carriers and photons associated with higher-order modes,[15] or fabricating gratings on ridge waveguides for simultaneous transverse and longitudinal mode selection.[16,17] These methods, however, lack precision in mode discrimination and struggle to maintain stable fundamental mode operation, compounded by the technical challenges of deep etching

†Corresponding author. E-mail: lantian9094@bjut.edu.cn

‡Corresponding author. E-mail: liuxuesheng@bjut.edu.cn

© 2026 Chinese Physical Society and IOP Publishing Ltd. All rights, including for text and data mining, AI training, and similar technologies, are reserved.

processes.

In comparison, supersymmetry serves as an effective approach to control the stable fundamental mode output in wide waveguides. Supersymmetry (SUSY) theory in quantum mechanics has emerged as a powerful tool for EEL waveguide design, and SUSY designs are categorized into two design schemes based on single-tube and array configurations for the main waveguide.[18–23] However, the power of supersymmetric lasers remains only at the level of hundreds of milliwatts.[24,25] At the same time, applications of supersymmetry in tapered lasers are still underexplored. Therefore, combining supersymmetry with tapered designs presents a promising approach to achieving high-power single-mode operation.

In this paper, we propose a novel segmented single-mode tapered laser architecture leveraging SUSY theory. This design systematically correlates main ridge geometries with supersymmetric sub-waveguide configurations across different sections. Using the coupled-mode theory, we optimize the spacing between sub-waveguides to maximize mode discrimination between fundamental and higher-order modes. Furthermore, phase-shifted gratings are integrated between tapered sections to enable simultaneous longitudinal mode selection and higher-order lateral mode suppression. This approach provides a robust framework for developing on-chip integrated high-power fundamental-mode tapered lasers.

2. Calculation and simulation

As the waveguide width increases, the number of supported modes within the waveguide also rises. To determine an optimal tapered waveguide structure, we employ theoretical calculation methods to analyze the cut-off condition for a waveguide mode. The waveguide structure of semiconductor lasers is typically modeled as a three-layer waveguide. The cut-off condition for a waveguide mode refers to the critical point at which a specific mode ceases propagating. This condition is determined by the waveguide's geometric parameters, refractive index contrast of materials, and the operating wavelength. Additionally, a ridge width mode sweep was performed in the software simulation to establish the relationship between ridge width and mode propagation constants. As shown in Fig. 1, combining the results from calculation, the number of supported modes progressively increases from 2 to 4 for ridge widths of 8 μm, 12 μm and 16 μm. These widths were therefore selected as the terminal dimensions for the three-segment tapered waveguide.

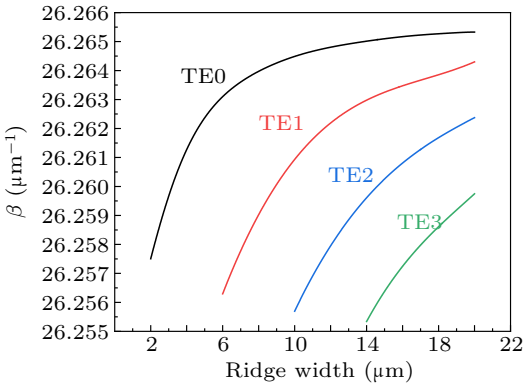


Fig. 1. Dependence of mode propagation constants β of four typical transverse modes, i.e., TE0, TE1, TE2, TE3, in relationship with the ridge width.

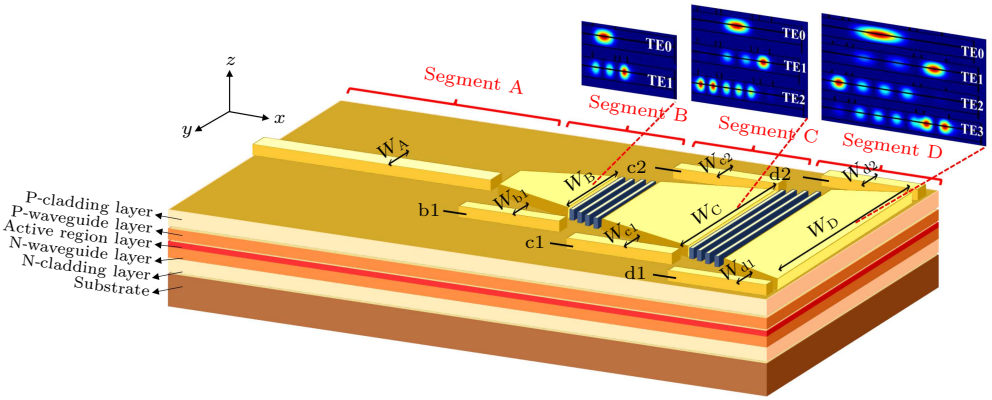


Fig. 2. Schematic diagram of the designed segmented supersymmetric tapered laser, including one ridge waveguide A and three supersymmetric structures, denoted as segments B, C and D.

The proposed segmented tapered laser structure consists of a ridge waveguide of 1000 μm in length, followed by a 3000 μm length of tapered waveguide. As depicted in Fig. 2, it comprises four distinct sections: section A features a ridge waveguide with a width of $W_A = 3$ μm, serving as the seed source; section B integrates a tapered waveguide of width $W_B = 8$ μm alongside a supersymmetric waveguide b1 with $W_{b1} = 2.67$ μm; section C incorporates a tapered waveguide of width $W_C = 12$ μm, flanked by supersymmetric waveguides c1 and c2 with widths $W_{c1} = 4.82$ μm and $W_{c2} = 7.13$ μm; and section D includes a tapered waveguide of width $W_D = 16$ μm, paired with supersymmetric waveguides d1 and d2 with widths $W_{d1} = 6.63$ μm and $W_{d2} = 3.68$ μm, respectively. Two phase shifting gratings designed for the cen-

tral wavelength of 808 nm are sandwiched between segments to enable longitudinal mode selection. The seed laser generated in the ridge waveguide undergoes amplification in the tapered regions, while the supersymmetric waveguides suppress higher-order modes through selective loss, and the phase shifting gratings filter longitudinal modes. This synergistic design achieves high-power output with exceptional beam quality in the fundamental mode.

2.1. Phase-shifted grating design

During the operation of on-chip integrated lasers, the multi-longitudinal-mode phenomenon is highly prevalent due to various specific structural designs. Researchers typically employ a distributed Bragg reflector (DBR) to achieve single-longitudinal-mode output.[26–28] However, for the laser design in this work, reflecting the target wavelength would prevent its propagation within the resonant cavity. And unlike the DBR gratings, phase-shifted gratings could transmit the target wavelength while reflecting others to meet our requirement of longitudinal mode selection.

Compared to conventional DBR structures, phase-shifted gratings incorporate a phase shift layer within the periodic grating structure. This introduced phase shift layer induces a phase shift in light satisfying the Bragg condition, thereby creating a low-reflectivity window within the grating's high-reflectivity spectrum. In the grating simulation, we employ a multilayer thin-film model to investigate the specific structural design of the phase-shifted grating.

Firstly, for the traditional DBR structure, the grating width is calculated as

$$d_i = \frac{m\lambda}{2n_{\text{eff}}}x, \tag{1}$$

where m is the grating order, n_{eff} is the effective refractive index, and x is the grating duty cycle.

Based on the grating structural parameters, the transfer matrix for each layer can be then calculated. The transfer matrix M_i is given by[29]

$$M_i = \begin{bmatrix} \cos\frac{2\pi n_i}{\lambda}d_i & -\mathrm{j}\frac{1}{n_i}\sin\frac{2\pi n_i}{\lambda}d_i \\ -\mathrm{j}n_i\sin\frac{2\pi n_i}{\lambda}d_i & \cos\frac{2\pi n_i}{\lambda}d_i \end{bmatrix}, \tag{2}$$

where n_i is the effective index of the i-th layer, d_i is the width of the i-th layer.

To open a transmission window spectrally within the grating, the introduction of a phase shift layer is then needed. The transmission matrix of the phase shift layer M_{s} is as follow:

$$M_{\text{s}} = \begin{bmatrix} \mathrm{e}^{\mathrm{j}\phi_{\text{s}}} & 0 \\ 0 & \mathrm{e}^{-\mathrm{j}\phi_{\text{s}}} \end{bmatrix}, \tag{3}$$

where ϕ_{s} is the phase shift.

Thus, the final system transfer matrix M of the grating, derived from Eq. (3), is

$$M_{\text{t}} = (M_1M_2)^q M_{\text{s}}(M_1M_2)^{N-q} = \begin{bmatrix} A & C \\ B & D \end{bmatrix}, \tag{4}$$

where N denotes the number of grating pairs, q denotes adding a phase shift layer after the q-th pair of gratings.

After obtaining the system transfer matrix, the reflection coefficient R is calculated using

$$R = \left| \frac{n_i \times (A + n_{i+1} \times B) - C - n_{i+1} \times D}{n_i \times (A + n_{i+1} \times B) + C + n_{i+1} \times D} \right|. \tag{5}$$

We utilize Eqs. (1)–(5) to design phase shifting gratings to achieve longitudinal mode selection and structural connection.

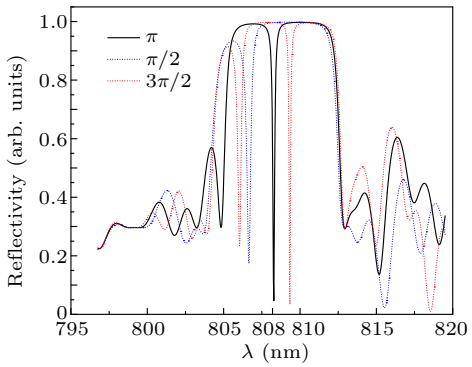


Fig. 3. Wavelength-dependent grating reflectivity for the designed phase-shifted grating structure in the supersymmetric segmented tapered laser with the lowest reflectivity occurring at the desired 808 nm.

Figure 3 shows the spectrum of phaser shifting gratings with variation of ϕ_{s}. As shown in the figure, when $\phi_{\text{s}} = \pi$ the center wavelength of the transmission peak in the phase-shifted grating spectrum coincides precisely with the target wavelength. As ϕ_{s} decreases, the transmission peak shifts toward shorter wavelengths. Conversely, as ϕ_{s} increases, the peak shifts toward longer wavelengths, eventually resulting in two distinct transmission windows at larger phase shifts. Because when $\phi_{\text{s}} = \pi$, the induced phase shift equals half the grating period. This configuration optimally locates the defect mode at the center of the bandgap, thereby generating a narrow transmission peak that matches exactly with the designed wavelength. As ϕ_{s} deviates from π, the optical path difference introduced by the phase shift changes, thereby altering the resonant condition. A smaller ϕ_{s} effectively shortens the cavity length, blue-shifting the resonance, while a larger ϕ_{s} increases the effective length, resulting in a red shift.

Ultimately, the grating is designed with a period of 2.397 μm, a grating order of 20, and a duty cycle of 0.5. The grating comprises 21 pairs, with a 17.9 μm phase shift layer inserted after the tenth pair. This phase shift layer consists of an unetched material identical to that of the waveguide layer.

2.2. Sub-waveguide design

In supersymmetry theory, SUSY sub-waveguides are engineered to mode-match with the higher-order modes of the main waveguide, thereby elevating their lasing thresholds and enabling stable fundamental mode operation. Figure 4 illustrates the mode-matching between the main waveguide and sub-waveguide, where the mode pairs marked within the red dashed box represent the lossy modes.

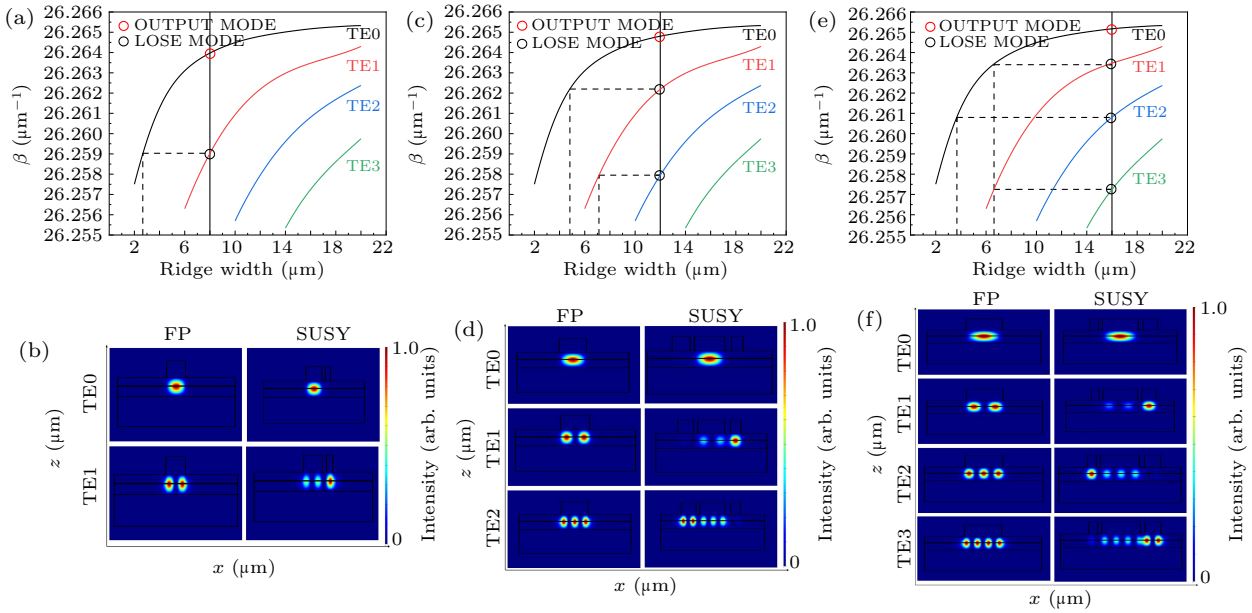


Fig. 4. (a) Mode-matching diagram of $TE1_B/TE0_{b1}$; (b) comparison between modes supported by traditional FP and supersymmetric structure B; (c) mode-matching diagram of $TE1_C/TE0_{c1}$ and $TE2_C/TE0_{c2}$; (d) comparison between modes supported by traditional FP and supersymmetric structure C; (e) mode-matching diagram of $TE1_D/TE0_{d1}$, $TE3_D/TE1_{d1}$ and $TE2_D/TE0_{d2}$; (f) comparison between modes supported by traditional FP and supersymmetric structure D; the coupled loss mode pairs are enclosed in the red dashed boxes.

The emission facet in segment B supports two modes: $TE0_B$ and $TE1_B$. Based on the matching relationship depicted in Fig. 4(a), a supersymmetric waveguide b1 with a width of 2.67 μm was designed. The $TE0_{b1}$ mode supported by b1 forms a coupling pair with the $TE1_B$ mode, thereby increasing the lasing threshold of the $TE1_B$ mode. In contrast, the $TE0_B$ mode exhibits no mode matching with the modes in supersymmetric waveguide B, leaving its threshold unaffected. Figure 4(b) illustrates the waveguide mode distribution, demonstrating that the $TE1_B$ mode in the main waveguide couples with the $TE0_{b1}$ mode in supersymmetric waveguide b1, while the fundamental mode remains undisturbed.

And the emission facet in segment C supports three modes: $TE0_C$, $TE1_C$, and $TE2_C$. Based on the mode-matching relationships illustrated in Fig. 4(c), supersymmetric waveguides c1 and c2 were designed with widths of 4.82 μm and 7.13 μm, respectively. The $TE0_{c1}$ mode supported by waveguide c1 forms a coupling pair with the $TE1_C$ mode in the main waveguide, while the $TE1_{c2}$ mode in waveguide c2 couples with the $TE2_C$ mode in the main waveguide. This configuration effectively increases the lasing thresholds of the higher-order modes. Figure 4(d) demonstrates the coupling interactions: the $TE1_C$ and $TE2_C$ modes in the main waveguide couple with the $TE0_{c1}$ mode in supersymmetric waveguide c1 and the $TE1_{c2}$ mode in supersymmetric waveguide c2, respectively, resulting in enhanced mode selectivity and suppressed high-order mode lasing.

Similarly, the emission facet in section D supports four modes. Based on the mode-matching relationships shown in Fig. 4(e), a supersymmetric waveguide d1 with a width of 6.63 μm was designed to suppress the $TE1_D$ and $TE3_D$ modes, while a supersymmetric waveguide d2 with a width of 3.68 μm was implemented to attenuate the $TE2_D$ mode. As depicted in Fig. 4(f), the $TE1_D$ and $TE3_D$ modes form coupling pairs with the fundamental and first-order modes of supersymmetric waveguide d1, respectively, and the $TE2_D$ mode couples with the fundamental mode of supersymmetric waveguide d2. This design effectively raises the lasing thresholds of higher-order modes, ensuring robust fundamental-mode operation. In this model, we ignored the thermal effects and their consequent impact on carrier dynamics.

3. Analysis and optimization

The optical loss in semiconductor lasers is governed by the imaginary part of the mode propagation constant β''. For a waveguide structure with active gain material, β'' relates to the material gain or loss through the mode limiting factor Γ and the imaginary part of the refractive index n''.[30] The specific relation is

$$\beta'' = \frac{2\pi\Gamma n''}{\lambda}, \tag{6}$$

where Γ is the mode limiting factor, which represents the proportion of light wave energy in the core region.

Figure 5 illustrates the mode interactions within the supersymmetric structure. Figures 5(a)–5(c) depict the mode-matching relationships across the three segmented waveguide sections. Figure 5(a) shows that within the 8 μm-wide main waveguide, TE_M remains unaffected, while TE_{M1} forms a coupling pair with the fundamental mode of the subsidiary waveguide, increasing its excitation threshold. As a result, higher-order modes are less likely to be excited during operation. Notably, in this case, mode TE_{R1} appears in the subsidiary waveguide. Although there is no matching mode in the main

waveguide, the subsidiary waveguide does not provide pumping in the actual laser operation. Therefore, this mode cannot lase and does not affect the fundamental mode output of the laser. Similarly, higher-order modes in the 16 μm-wide main waveguide also correspond to modes in the subsidiary waveguides. In conclusion, these subfigures demonstrate that all higher-order modes, except the fundamental mode, form coupling pairs with modes in the SUSY sub-waveguides, effectively raising their lasing thresholds. To quantify the resulting model loss differential induced by the elevated thresholds, we modeled the active region with a complex refractive index in our simulation software. This approach allowed us to simulate the practical operational losses in both conventional Fabry–Perot (FP) cavities and SUSY-based structures. Figure 5(d) compares the model losses between these configurations. In the conventional FP cavity, all modes exhibit similarly low losses. However, with the SUSY structure, losses for higher-order modes increase significantly, while the fundamental mode remains unaffected. This behavior stems from the coupling pairs formed between the SUSY sub-waveguides and the main waveguide, which selectively enhance the thresholds of higher-order modes. The minimum observed loss differential for higher-order modes is 8.03 cm^{-1}, underscoring the efficacy of the SUSY design in suppressing unwanted modes while preserving fundamental mode stability.

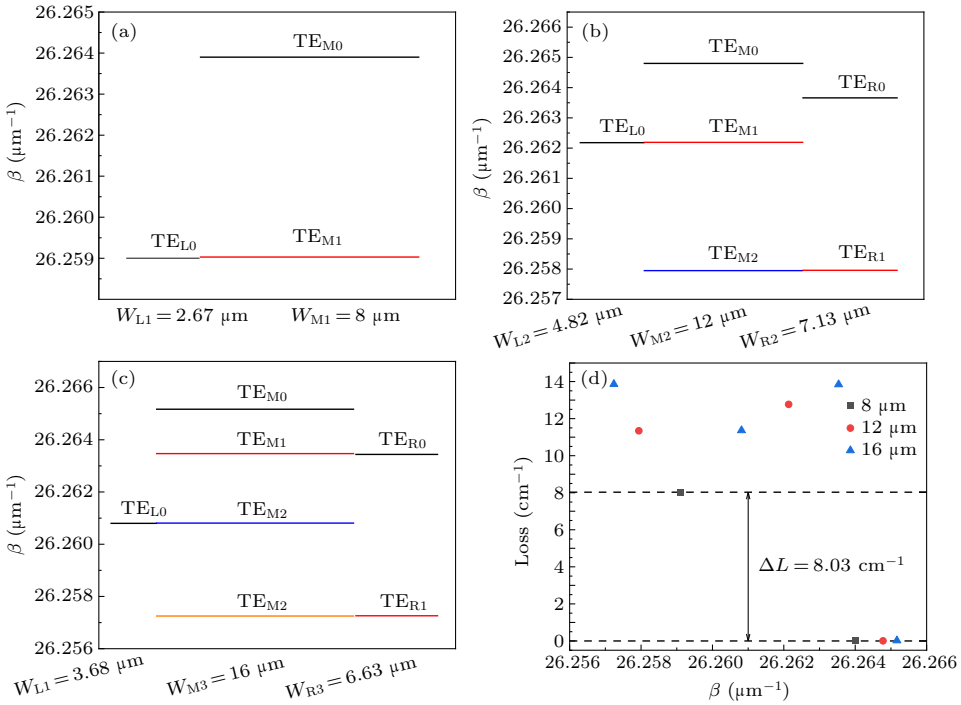


Fig. 5. SUSY structure mode-matching relationships: (a) segment B; (b) segment C; (c) segment D; (d) loss of different modes supported by SUSY structure and traditional FP.

Additionally, we analyze the influence of waveguide spacing on the coupling coefficient based on the coupled-mode theory and determine the optimal spacing design considering practical fabrication constraints.

The coupling between the modal fields of the waveguides occurs via evanescent waves. Let a_i represent the electric field amplitudes of the two waveguides. The coupled-mode equations can be expressed as

$$\begin{cases} \frac{\mathrm{d}a_1}{\mathrm{d}z} = -\mathrm{j}\beta_1 a_1 - \mathrm{j}\kappa_{12} a_2, \\ \frac{\mathrm{d}a_2}{\mathrm{d}z} = -\mathrm{j}\beta_2 a_2 - \mathrm{j}\kappa_{21} a_1, \end{cases} \tag{7}$$

where κ_{mn} is the coupling coefficient from waveguide n to waveguide m. The expression for is given by

$$\kappa_{mn} = \frac{k_0^2}{2\beta_m} \frac{\int_{G_m} (\varepsilon_m - \varepsilon_n) U_m^* \cdot U_n \,\mathrm{d}A}{\int |U_m|^2 \,\mathrm{d}A}, \tag{8}$$

where $\varepsilon_m - \varepsilon_n$ is the background dielectric constant difference, $U_m^* \cdot U_n$ represents the overlap of the two modal fields, and the integration domain G_m corresponds to the perturbed region.

For asymmetric waveguides, the coupling coefficient κ is calculated as[31]

$$\kappa = \sqrt{\kappa_{mn} \cdot \kappa_{nm}}. \tag{9}$$

Based on the aforementioned theory, MATLAB simulations are conducted. Figure 6 illustrates the coupling coefficients between each super-symmetric waveguide and the corresponding main waveguide as a function of spacing. As the spacing increases, the coupling coefficient exhibits a gradual decline. Furthermore, wider waveguides achieve higher coupling coefficients at the same spacing. This is attributed to their broader modal field distribution, which enhances the overlap integral region during evanescent wave coupling. Considering practical fabrication challenges and cost constraints, the inter-waveguide spacing was optimized to 1.2 μm. At this

width, the mode coupling efficiency remains relatively high, exceeding 0.65. Moreover, in terms of practical fabrication processes, an etching width of 1.2 μm is achievable with electron beam lithography (EBL), ensuring the feasibility of the structure.

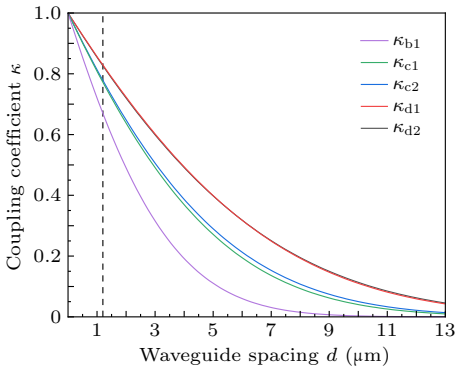


Fig. 6. Inverse correlation between the waveguide spacing d and coupling coefficient κ in diverse SUSY structures.

4. Conclusion and perspectives

In summary, we proposed a novel segmented fundamental-mode tapered laser based on supersymmetry theory to address the long-standing challenge of transverse mode instability in conventional tapered edge-emitting devices. By integrating three-stage longitudinal taper waveguides with asymmetric supersymmetric sub-waveguides, each segmented tapered waveguide successfully couples with high-order transverse modes. This design elevates the lasing threshold of higher-order modes beyond that of the fundamental mode, thereby achieving robust single-mode operation. Additionally, we also analyzed the influence of inter-waveguide spacing on coupling coefficients using coupled-mode theory, and selected an optimal spacing of 1.2 μm by considering practical fabrication constraints. A phase-shifted grating designed via the transfer matrix method was further implemented for longitudinal mode selection and structural interconnection. Compared with conventional tapered lasers, this innovative design offers enhanced stability in mode selection, providing a new paradigm for designing on-chip integrated high-power fundamental-mode tapered lasers. Future efforts will focus on developing supersymmetric structures that evolve with the tapered waveguide profile through advanced waveguide theory exploration, aiming to realize synchronous mode coupling throughout the device.

Acknowledgement

This research was funded by the Science and Technology Commission Foundation of the Central Military Commission of China (Grant No. 2023-JCJQ-JJ-1008).

References

[1] Zhang W, Liu W, Wang J, Cao P, Chen J, Ting F, Zhou X and Zheng W H 2022 *Opt. Lett.* **47** 5012
[2] Liu S, Li Z, Zhou S, Luo X, Meng Y, Wu W, Feng C and Zhang J 2024 *Opt. Commun.* **564** 130631
[3] Liu Z W, Liu S P, Wang C L, Zhao F, Xing W, Xiong C, Zhu L N and Ma X Y 2024 *Opt. Lett.* **49** 3448
[4] Xiang M W, Zhang Y H, Li G J, Liu C, Chen Q N, Lu Q Y, Huang L R, Lu M Z, DoneGan J and Guo W H 2022 *Opt. Express* **30** 30187
[5] Chang J Y, Xiong C, Qi Q, Hao S, Liu S P and Ma X Y 2023 *IEEE Photonics Technology Letters* **35** 862
[6] Qi J, Lan T, Ma W L, Zhang J H, Li Y, Li D, Liu X S and Wang Z Y 2024 *Optics & Laser Technology* **177** 111168
[7] Zhang N Y, Qiu B C, Zou Y G, Fan J, Yue Y X, Song Y M, Ren Z Q, Li Q M and Ma X H 2024 *IEEE Photonics Technology Letters* **36** 1217
[8] Pinto D, Díaz Thomas D A, Loghmari Z, Kinjalk K, Teissier R, Bahriz M, Lendl B and Baranov A N 2024 *Opt. Express* **32** 26925
[9] Lv M Y, Zhou Z Y, He Y W, Xie P F, Li Y, Wang H M, Du W C, Gao S X, Tang C and Wu D Y 2025 *Opt. Express* **33** 897
[10] Tijero J M G, Odriozola H, Borruel L, Esquivias I, Sujecki S and Larkins E C 2007 *IEEE Photonics Technology Letters* **19** 1640
[11] Sumpf B, Hasler K.H, Adamiec P, Bugge F, Dittmar F, Fricke J, Wenzel H, Zorn M, Erbert G and TrÄnkle G 2009 *IEEE Journal of Selected Topics in Quantum Electronics* **15** 1009
[12] Ostendorf R, Kaufel G, Moritz R, Mikulla M, Ambacher O, Kelemen M T and Gilly J 2008 *High-Power Diode Laser Technology and Applications VI* **6876** 146
[13] Paschke K, Sumpf B, Dittmar F, Erbert G, Staske R, Wenzel H and Trankle G 2005 *IEEE Journal of selected topics in quantum electronics* **11** 1223
[14] Müller A, Fricke J, Bugge F, Brox O, Erbert G and Sumpf B 2016 *In-Plane Semiconductor Lasers XV* **9767** 193
[15] Li J, Qiu Y T, Cao Y H, Qin W B, Liu Y Q, Zeng X, Yan A and Wang Z Y 2018 *Optik* **158** 502
[16] Kuusela L, Aho T, Ulkuniemi R, Mähönen M, Hämelahti J, Schramm A, Talmila S, Sipilä P and Uusimaa P 2024 *In-Plane Semiconductor Lasers XXIII* **12905** 54
[17] Yang J J, Fan J, Zou Y G, Wang H Z and Ma X H 2022 *Chin. Phys. B* **31** 084203
[18] Hokmabadi M.P, Nye N.S, El-Ganainy R, Christodoulides D N and Khajavikhan M 2019 *Science* **363** 623
[19] Jin Y H, Zhu B F, Tan K H, Wicaksono S, Sirtori C, Yoon S F and Wang Q J 2024 *Appl. Phys. Lett.* **124** 111109
[20] Qiao X D, Midya B, Gao Z H, Zhang Z F, Zhao H Q, Wu T W, Yim J, Agarwal R, Litchinitser N M and Feng L 2021 *Science* **363** 403
[21] Wang L C, Wang Y F, Dong F X, Fu T, Li M N, Zhang K, Gong K, Zhou X Y and Zhang J X 2024 *Opt. Lett.* **49** 3078
[22] Xu Y B, Fu T, Fan J, Liu W Z, Qu H W, Wang M J and Zheng W H 2023 *Photonics* **10** 238
[23] Miri M.A, Heinric M, El-Ganainy R and Christodoulides D N 2013 *Phys. Rev. Lett.* **110** 233902
[24] Wang Z, Fan J, Zou Y, Fu X, Shi L, Li Y and Ma X 2025 *Opt. Commun.* **577** 131425
[25] Fu T, Chen J X, Wang Y F, Zhou X Y, Qi A Y, Wang X Y, Dai Y Q, Wang M J and Zheng W H 2023 *Opt. Express* **31** 1858
[26] Yamaoka K, Ariga M, Terada Y, Mikhailov V, Ishii H, Kimura T and Kurobe T 2024 In 2024 *IEEE 29th International Semiconductor Laser Conference (ISLC)* (1–2) IEEE
[27] Ulkuniemi R, Kuusela L, Mähönen M, Aho T, Hämelahti J, Schramm A, Talmila S, Sipilä P and Uusimaa P 2024 *Quantum Computing, Communication and Simulation IV* **12911** 332
[28] Müller A, Maiwald M and Sumpf B 2022 *In-Plane Semiconductor Lasers XXI* **12021** 8
[29] Liu Y, Chen D, Duan F and Yu Y 2022 *Optics & Laser Technology* **149** 107830
[30] Ma Y, Lan T, Wang X, Ruan R, Cao Y, Dai J and Wang Z 2022 *Opt. Express* **30** 9892
[31] Coldren L A, Corzine S W and Mashanovitch M L 2012 *Diode lasers and photonic integrated circuits* 212